CRYSTAL GROWTH & DESIGN

pubs.acs.org/crystal

Article

Lanthanide(III) Cation Size Selective Formation of Two Different Metal−Organic Frameworks

Narhari Sapkota, Ermei Mäkilä, Ari Lehtonen, and Anssi Peuronen*

Cite This: *Cryst. Growth Des.* 2025, 25, 3119−3127

Read Online

ACCESS | Metrics & More | Article Recommendations | Supporting Information

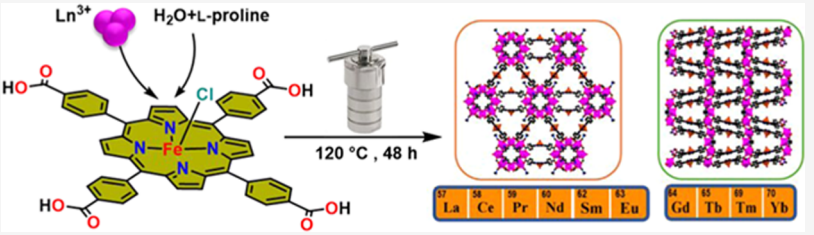

ABSTRACT: The reaction between a 5,10,15,20-tetrakis(4-carboxyphenyl) porphyrin-FeCl linker (TCPP-Fe) and lanthanide ions (Ln^{3+}) in excess of L-proline coligand provides a synthetic route to two structurally different metal−organic frameworks (TCPP-$FeOH_{0.5}/H_2O_{0.5}$)(L-proline)$_2Ln_2(H_2O)(DMF)_{0.5}$ (where Ln = La^{3+}, Ce^{3+}, Pr^{3+}, Nd^{3+}, Sm^{3+}, and Eu^{3+}) and (TCPP-FeOH)(L-proline)$Ln_{1.5}$ (where Ln = Gd^{3+}, Tb^{3+} Tm^{3+} and Yb^{3+}). The selection between the two different structures is dependent on the lanthanide ion atomic number. From the different Ln^{3+} ions used in this study, early-to-mid lanthanides, La^{3+}, Ce^{3+}, Pr^{3+}, Nd^{3+}, Sm^{3+}, and Eu^{3+}, give a structure consisting of discrete Ln_8 building units (**1-Ln**), while mid-to-late lanthanides, Gd^{3+}, Tb^{3+}, Tm^{3+}, and Yb^{3+}, give a framework built upon one-dimensional Ln^{3+} chains (**2-Ln**). Therefore, the size of the lanthanide ion seems to play a key role in the structure selection and stability, which contrast with the commonly accepted behavior of lanthanides. Activation and subsequent argon gas sorption analyses done using **1-Nd** and **2-Tb** showed that **1-Nd** is permanently porous with a determined surface area of 1223 ± 4 m^2/g, while **2-Tb** undergoes a structural change significantly decreasing its surface area (236 m^2/g) from its expected value (ca. 900 m^2/g). Stability tests on the activated samples revealed that **1-Nd** lost its crystallinity after 1 month of exposure to atmospheric moisture, whereas **2-Tb** retained its crystallinity, underscoring the higher long-term stability of **2-Tb** compared to that of **1-Nd**.

INTRODUCTION

Metal−organic frameworks (MOFs) are multifunctional porous materials that have gained tremendous attention from both academic and industrial fields.[1−3] The main features of MOFs are their porosity, large surface area, tunable pore size, framework flexibility, and structural diversity, which make them suitable materials for various applications. The potential applications of MOFs range from catalysis,[4] energy storage,[5] and storage/separation of valuable or undesirable gases, ions, or molecules.[6−8] For example, the separation of hydrocarbons depends on the pore size and functionality of the adsorbent, achievable by tailoring the structural features of MOFs.[9] The most intriguing feature of MOFs is their structural modifiability, which is in stark contrast to traditional inorganic adsorbents such as zeolites. It can be envisioned that an immeasurable number of distinct MOF structures can be assembled by using different inorganic metal ions/nodes and organic ligands/linkers in various combinations.

In the design of MOF materials, lanthanide MOFs (Ln-MOFs) have become increasingly popular due to their unique properties, such as highly efficient luminescence and activity as heterogeneous catalysts.[10−12] In contrast to d-block transition metals with rather predictable coordination numbers (CN) and geometries, lanthanides, with high and variable coordination numbers (CN = 6−12) and flexible coordination environments, provide a greater challenge in designing framework architectures with predetermined structures.[13] Furthermore, compared to transition-metal ions, lanthanide ions have bonds with more ionic character, making them less directional and leading to more varied coordination geometries[14,15] and structures with diverse topologies.[14,16] The design and construction of highly connected MOFs has attracted much attention not only because of their intriguing structures and topologies but also for their potential applications in many fields due to their enhanced stability and stable porosity.[17] It has been reported that the lanthanide ions can be coordinated by up to eight N-oxide donors without

Received: February 6, 2025
Revised: April 9, 2025
Accepted: April 9, 2025
Published: April 15, 2025

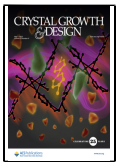

https://doi.org/10.1021/acs.cgd.5c00153
Cryst. Growth Des. 2025, 25, 3119−3127

imposing severe steric constraints on the metal center,[18] which demonstrates that highly connected MOFs can be constructed using lanthanides without significant loss of stability. Differences in the coordination behavior of Ln^{3+} ions are sometimes observed due to their different ionic radii, which decrease with increasing atomic number and can influence the coordination number and lead to diversity in the crystal structure and physical properties. Therefore, it is meaningful to investigate whether an architecture obtained with a particular Ln^{3+} cation is maintained across the entire lanthanide series. To date, there are a few reports available on the diversity of Ln-based structures controlled by the size of the Ln^{3+} ions.[19−22]

It is well-known that Ln^{3+} ions have high affinity toward hard donor atoms, thus multidentate ligands with oxygen donor atoms are widely used in the construction of lanthanide-containing coordination polymers.[23] In this regard, having multiple carboxylate binding sites, highly symmetric planar aromaticity, high rigidity, and potential for rich redox chemistry makes metal porphyrin carboxylates as ideal organic linkers to build Ln-MOFs.[24] If a coligand is introduced in the system along with a multicarboxylate ligand, cooperativity of both ligands with different coordination modes can provide a route to new Ln-MOFs.[25] In addition to structural variation, mixed-ligand systems can also provide a route to new properties, such as adding chirality to MOFs.[26]

In this work, we report the synthesis of lanthanide ion (La^{3+}, Ce^{3+}, Pr^{3+}, Nd^{3+}, Sm^{3+}, Eu^{3+}, Gd^{3+}, Tb^{3+}, Tm^{3+}, Yb^{3+})-based MOFs with Fe-porphyrin tetracarboxylate as a linker and L-proline as a secondary ligand (coligand). In contrast to benzoic acid, used for example in CAU-19 series of lanthanide and porphyrin-based MOFs,[27] L-proline, although similar to benzoic acid in size, can act as a ditopic ligand, which has a profound effect on the MOF network structure. Furthermore, it may also have different properties as a modulator in the self-assembly reaction leading to framework formation. We show that under the defined synthesis conditions, the differences in lanthanide ionic radii give rise to two different MOF structures, which appear as needle-shaped and plate-shaped crystals. These two MOF structures (TCPP-$FeOH_{0.5}/H_2O_{0.5}$)(L-proline)$_2Ln_2(H_2O)(DMF)_{0.5}$ and (TCPP-FeOH)(L-proline)-$Ln_{1.5}$ both incorporate L-proline, which acts as a bridging ligand in the lanthanide metal SBUs to form either infinite chains or eight-membered rings.

EXPERIMENTAL SECTION

Methods and Materials. Lanthanide (La^{3+}, Ce^{3+}, Pr^{3+}, Nd^{3+}, Sm^{3+}, Eu^{3+}, Gd^{3+}, Tb^{3+}, Tm^{3+}, and Yb^{3+}) nitrates, *N*,*N*-dimethylformamide (DMF), L-proline, and methyl 4-formylbenzoate were purchased from Merck and were used without further purification. Pyrrole (Merck) was distilled before use. 5,10,15,20-Tetrakis((4-methoxycarbonyl)phenyl) porphyrin-FeCl and 5,10,15,20-tetrakis(4-carboxyphenyl) porphyrin-FeCl (TCPP-FeCl) were prepared according to the previously reported procedures.[28,29] IR spectra of the ligand precursor and MOFs were recorded on a Bruker VERTEX 70 FTIR spectrometer in the 4000−400 cm^{-1} region. Thermal analyses were performed on a TA Instruments SDT Q600 simultaneous thermogravimetric analysis (TGA)-differential scanning calorimetry (DSC) apparatus between 30 and 1000 °C in a N_2 flow using an aluminum oxide pan as the sample holder. A flow rate of 50 mL/min and heating rate of 10 °C/min were maintained throughout the measurements. Powder X-ray diffraction (PXRD) data were collected with a Panalytical Aeris Research Edition powder X-ray diffractometer with Bragg−Brentano geometry equipped with a PIXcel^{1D} detector using Cu $K_{\alpha1,\alpha2}$ radiation ($\lambda_{\alpha1}$ = 1.5406, $\lambda_{\alpha2}$ = 1.5444 Å). The samples were prepared on a zero background Si disc and rotated 60 rpm during data collection. Pawley fitting of the PXRD data was carried out using the Malvern Panalytical HighScore Plus v4.9 software.[30] Argon adsorption isotherms were obtained at −196 °C with a 3Flex 3500 instrument (Micromeritics Corp., USA). The apparent specific surface area was calculated using the Brunauer−Emmett−Teller (BET) method, while the pore volume was estimated using the Gurvich rule, taking the total adsorbed amount when the isotherm showed an uptake plateau. The pore size distribution was calculated with MicroActive v5.01 software (Micromeritics Corp.) using density functional theory (DFT) with a zeolite model, assuming the pore shape as cylindrical. Before the adsorption experiments, the samples were degassed at 120 °C for 2 h followed by 12 h at 60 °C in VacPrep 061 (Micromeritics Corp.) at 10^{-3} mbar. Prior to the measurement, the samples were further outgassed in situ for 2 h at 120 °C in a 3Flex instrument at 10^{-5} mbar. Scanning electron microscope (SEM) images were obtained with Apreo S field-emission SEM (Thermo Scientific, The Netherlands) using an acceleration voltage of 2 kV. The samples were coated with 5 nm of Pt before imaging using a Q150 V ES+ sputter coater (Quorum Technologies Ltd., United Kingdom).

X-ray Crystallographic Details. Single-crystal X-ray diffraction data were collected with (1) Rigaku MicroMax-HF generator producing monochromatized Cu Kα radiation and HyPix-6000HE detector and (2) Bruker−Nonius Kappa APEX II diffractometer using Mo Kα radiation. Data collection and reduction of the Rigaku diffractometer data were done using the CrysAlis^{pro} software,[31] while COLLECT,[32] HKL Denzo, and Scalepack[33] were used for Bruker−Nonius data with the absorption correction applied using SADABS.[34] Crystal structures were solved and refined using SHELXS[35] and SHELXL[36] programs employing the OLEX2 interface.[37] Crystallographic data are presented in Table S1.

Refinement Details. **1-Nd** could be solved in the centrosymmetric space group *Cmmm* and in the noncentrosymmetric space group *C*222 from which the former showed 2-fold spatial disorder of the L-proline coligands and as a result, the latter was chosen for the refinement. Furthermore, one of the phenyl carboxylate moieties in **Nd-1** is disordered in a 1:1 ratio. C−C distances of these disordered C_6 rings, along with two others, were constrained with SADI, while the anisotropic displacement parameters of the respective C atoms were treated with RIGU, SIMU, and EADP where appropriate (EADP was applied to the disordered parts). In **2-Tb**, the L-proline coligand is disordered in approximately 1:2 ratio, and SADI and EADP were used in the refinement of the two parts. The atomic positions of the majority of uncoordinated solvent molecules within the pores of the crystal structures of **1-Nd** and **2-Tb** could not be refined, and the corresponding electron density was treated using the OLEX2 solvent mask procedure. The estimated number of solvent molecules are included in the empirical formulas of each of the crystal structures.

Crystal Data for $C_{92.5}H_{126}FeN_{17.5}Nd_2O_{27}$ (M = 2259.43 g/mol). Orthorhombic, space group *C*222 (no. 21), a = 25.7512(3) Å, b = 47.1679(6) Å, c = 16.94511(16) Å, V = 20582.1(4) Å^3, Z = 8, T = 100.01(17) K, μ(Cu Kα) = 9.376 mm^{-1}, D_{calc} = 1.458 g/cm^3, 34 692 reflections measured (3.91° ≤ 2θ ≤ 136.496°), 17 136 unique (R_{int} = 0.0359, R_{sigma} = 0.0494), which were used in all calculations. The final R_1 was 0.0556 ($I > 2\sigma(I)$) and wR_2 was 0.1671 (all data).

Crystal Data for $C_{74}H_{82}FeN_{12}O_{18}Tb_{1.5}$ (M = 1721.74 g/mol). Monoclinic, space group *P*2/*c* (no. 13), a = 17.4199(2) Å, b = 16.4243(3) Å, c = 26.3638(5) Å, β = 105.5525(11)°, V = 7266.8(2) Å^3, Z = 4, T = 170.0(10) K, μ(Mo Kα) = 1.724 mm^{-1}, D_{calc} = 1.574 g/cm^3, 65 575 reflections measured (3.208° ≤ 2θ ≤ 52.172°), 14 326 unique (R_{int} = 0.0636, R_{sigma} = 0.0607), which were used in all calculations. The final R_1 was 0.0543 ($I > 2\sigma(I)$) and wR_2 was 0.1316 (all data).

Synthetic Procedures. 25 mg portion (0.028 mmol) of TCPP-FeCl and 74−78 mg (0.17 mmol) of $Ln(NO_3)_3{\cdot}xH_2O$ (Ln = La^{3+}, Ce^{3+}, Pr^{3+}, Nd^{3+}, Sm^{3+}, Eu^{3+}, Gd^{3+}, Tb^{3+}, Tm^{3+}, and Yb^{3+}) were dissolved in 8 mL of DMF in a Pyrex tube by sonication, while 1.35 g (11.73 mmol) of L-proline was dissolved in 3 mL of water. The solutions were combined in a 20 mL poly(tetrafluoroethylene)

https://doi.org/10.1021/acs.cgd.5c00153
Cryst. Growth Des. 2025, 25, 3119−3127

Scheme 1. Synthetic Route to 1-Ln and 2-Ln

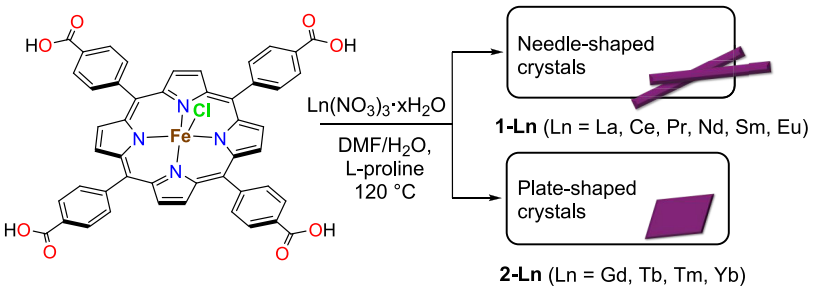

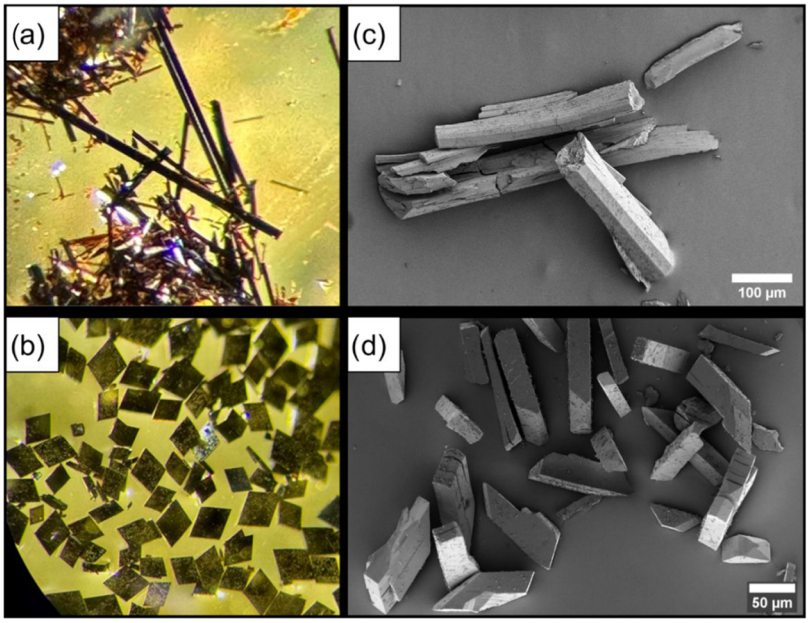

Figure 1. Optical (a, b) as well as electron micrographs (c, d) of needle-shaped **1-Nd** (top) and plate-shaped crystals **2-Tb** (bottom).

(PTFE)-lined steel reactor and incubated at 120 °C for 12 h and slowly cooled to room temperature. The formed dark needle- (**1-Ln**, where Ln = La^{3+}, Ce^{3+}, Pr^{3+}, Nd^{3+}, Sm^{3+}, and Eu^{3+}) or plate-shaped crystals (**2-Ln**, where Ln = Gd^{3+}, Tb^{3+}, Tm^{3+}, and Yb^{3+}) were collected and washed three times with DMF. The typical yields were in the range of 38−43% for **1-Ln** and 34−38% for **2-Ln**. The samples used in BET analyses were subjected to solvent exchange by immersion into chloroform for 3 days (chloroform was changed to a fresh batch every 12 h). The obtained crystals were thermally activated under high vacuum at 130 °C for 12 h for **1-Nd** and **2-Tb** MOFs.

RESULTS AND DISCUSSION

The solvothermal reaction between $Ln(NO_3)_3{\cdot}xH_2O$ and TCPP-FeCl in the presence of L-proline was carried out in a DMF/H_2O 8:3 mL mixture (Scheme 1). This reaction was found to yield two different types of crystals depending on which lanthanide ion was used. The early lanthanides, La^{3+}, Ce^{3+}, Pr^{3+}, Nd^{3+}, Sm^{3+}, and Eu^{3+}, gave dark needle-shaped crystals, whereas the later lanthanides, Gd^{3+}, Tb^{3+}, Tm^{3+}, and Yb^{3+}, yielded plate-shaped crystals (Figure 1). Interestingly, this change from needle- to plate-shaped crystals occurs at the middle of the lanthanide series and is most likely due to the different ionic radii of the Ln^{3+} ions[38] and the lanthanide contraction effect.[20,39] The morphological differences are also apparent at the microscopic level, as shown in the SEM images in Figure 1c,d (additional images in Figure S1).

The structure of needle-shaped crystals of **1-Nd** was solved in the chiral space group *C*222 by single-crystal X-ray diffraction. The crystal structure consists of three crystallographically unique Nd^{3+} ions, which together form a planar eight-membered Nd_8 ring, ca. 1.2 nm in diameter (Nd−Nd distance) where 16 TCPP-Fe linkers and eight L-proline coligands bridge the neodymium cations. While octanuclear lanthanide ring clusters are known, planar rings such as in **1-Nd** appear less common.[40,41] As shown in Figure 2, the Nd^{3+} coordination polyhedra are corner-sharing (Ln−O−Ln) in the inner ring, while the outer ring is bridged by Ln−(OCO)−Ln carboxylate bridges. Two of the Nd^{3+} cations have coordination number nine; Nd1 exhibits spherical capped square antiprism geometry according to calculated continuous shape measures (CShM),[42] while Nd2 has closest resemblance to muffin-type C_s-symmetric coordination geometry (Figure S2). In contrast, the coordination number of Nd3 is eight, while its geometry matches well with the biaugmented trigonal prism. The TCPP-Fe linkers form an hourglass-shaped structure with the Nd^{3+} cations where the Ph−COO^- groups face outward in ca. 137° angle above and below the Nd_8 plane (Figure 2c). The MOF three-dimensional (3D) network, which shows channels along the *a*- and *c*-axis directions as well as the *ab* diagonal, is built by each of the TCPP-Fe linking four distinct Nd_8 rings (Figure 2a). The N-donor atoms of the L-proline coligands are all coordinated to the Nd2 centers, while their carboxylate groups bridge between Nd2−Nd1 and Nd2−Nd3.

https://doi.org/10.1021/acs.cgd.5c00153
Cryst. Growth Des. 2025, 25, 3119−3127

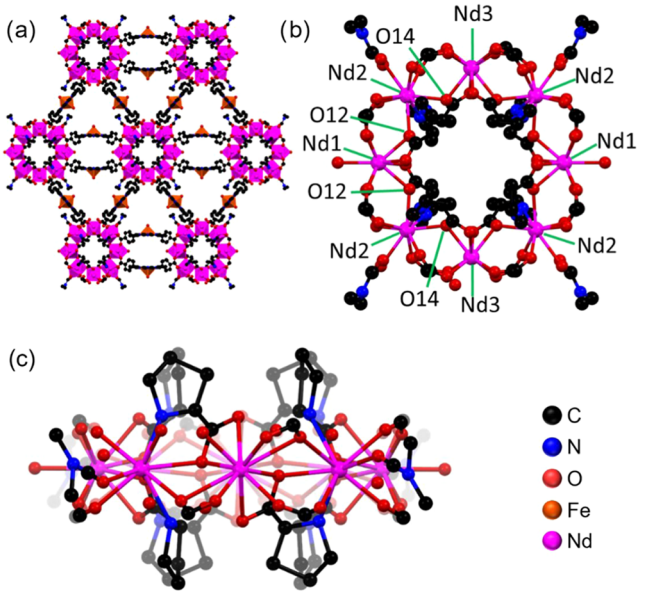

Figure 2. (a) View of the 3D polymeric structure of **1-Nd** along the *c*-axis. Ball-and-stick presentation of the Nd_8 ring in the structure of **1-Nd** viewed perpendicular (b) and along the Nd_8 plane (c).

Views perpendicular to and along the Nd_8 plane show that these L-proline coligands point opposite to the TCPP-Fe linkers with half of the L-proline molecules facing above and half below the Nd_8 plane (Figure 2b). Although the L-proline N−H protons could not be assigned from the residual electron density, the short d(N6−O15) = 3.11 Å and d(N7−O13) = 3.08 Å distances between the amine and carboxylate groups of adjacent L-proline coligands point to existing N−H···O hydrogen bonds and strongly suggest that the L-proline amine groups have not been deprotonated. In addition, partially disordered DMF and water molecules coordinate to Nd1 and Nd2 parallel to the Nd_8 plane. The refinement suggests that Cl^- anions, initially coordinated to Fe^{3+} centers, are cleaved from the TCPP-FeCl linkers during the solvothermal reaction since two distinct TCPP-Fe linkers exist in the MOF structure with either one or two O atoms coordinated to Fe ions. Based on the Fe−O bond lengths, the former can be interpreted as a square-pyramidal Fe^{3+}−OH complex [d(Fe2−O2) = 1.92 Å], whereas the latter is an octahedral Fe^{2+} with two water molecules coordinated to the axial positions [two equivalent d(Fe1−O1) = 2.08 Å bonds]. The interligand (TCPP-Fe) Fe−Fe distances of the two different channels are ca. 0.84 and 1.0−1.28 nm (Figure 2a). This interpretation provides a neutral net charge for the framework.

Plate-shaped crystals of **2-Tb** for the single-crystal structure analysis were obtained by the aforementioned solvothermal method. The structure was solved in a monoclinic crystal system with the space group $P2/c$. As **2-Tb** crystallizes in a centrosymmetric space group, it suggests that L-proline has undergone racemization. All Tb^{3+} ions in the structure are eight-coordinate but have two different coordination environments. Tb1 is coordinated to five TCPP-Fe linkers, two of which bridge between two Tb1 centers and two between Tb1 and Tb2 in Tb−(OCO)−Tb fashion, while one coordinates to Tb1 in bidentate mode. The respective triangular dodecahedron and square antiprism coordination polyhedra (based on CShMs) of Tb1 and Tb2 are corner-sharing between two Tb1 and one Tb2 where two proline coligands each provide one carboxylate O atom as the bridge, whereas the N-donor atoms of proline are coordinated solely to Tb2 (Figure S2). These groups of three corner-sharing coordination polyhedra are connected by carboxylate bridges at the Tb1 centers and thus form infinite one-dimensional (1D) chains along the *c*-axis of the unit cell. The TCPP-Fe linkers bind to four distinct lanthanide columns through the four carboxylate groups. Again, the Fe−Cl bond has been cleaved during the solvothermal process as OH^- anions are coordinated to the square-pyramidal Fe^{3+} centers [d(Fe−O) = 1.86 Å]. The TCPP-Fe linkers stack in pairs with the Fe−OH^- group pointing away from the adjacent porphyrin plane and are either coplanar or show an altering zigzag pattern when viewed along the crystallographic *b*- or *a*-axis, respectively (Figure 3a,d). The

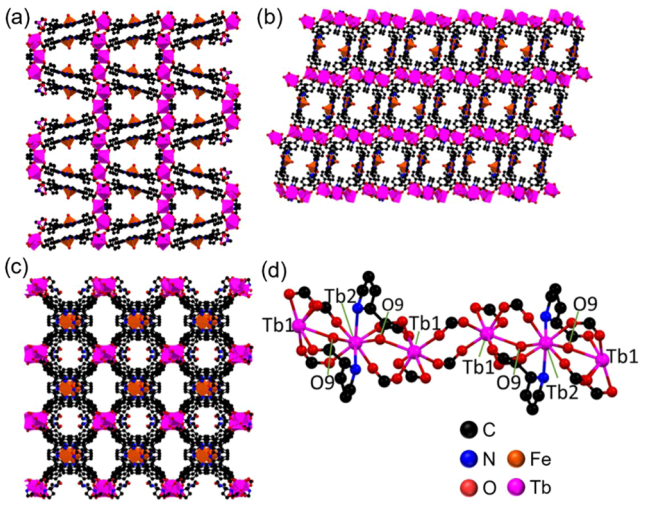

Figure 3. (a−c) 3D polymeric structure of **2-Tb** viewed along the *a*-axis, *b*-axis, and *c*-axis, respectively. (d) Ball-and-stick view of the one-dimensional SBU of **2-Tb**.

framework shows pores along all of the crystallographic main axes (Figure 3a−d), while the pore diameters (ca. 0.4−0.8 nm) are smaller compared to those of **1-Nd**. A comparison of the anionic charge provided by the ligands versus the cationic charge of the Tb^{3+} ions suggests that there is a surplus of −0.5 anionic charge per asymmetric unit. This could be explained by the presence of L-prolinium or $Me_2NH_2^+$ cations inside the network pores, of which the latter would be due to the decarbonylation of DMF solvent molecules during the solvothermal reaction. However, we could not reliably assign the unrefined electron density in the pores to either of these two species. Alternatively, the TCPP-Fe linker is a well-known redox-active species and could be partially oxidized, therefore balancing the charge of the framework.

PXRD was used to verify the bulk phase purity of the synthesized MOFs. The diffraction pattern of needle-shaped **1-Nd** is consistent with the pattern simulated from the respective crystal structure (Figure 4). Upon activation, i.e., removal of guest DMF and water molecules by solvent exchange and consequent heating under high vacuum, the structural integrity of **1-Nd** is maintained as evidenced by an excellent agreement between the diffraction patterns of the as-synthesized and activated materials. The bulk material of the plate-shaped **2-Tb** is also phase-pure and does not show diffraction peaks of the needle-shape phase (Figure 4). However, activation causes a

https://doi.org/10.1021/acs.cgd.5c00153
Cryst. Growth Des. 2025, 25, 3119−3127

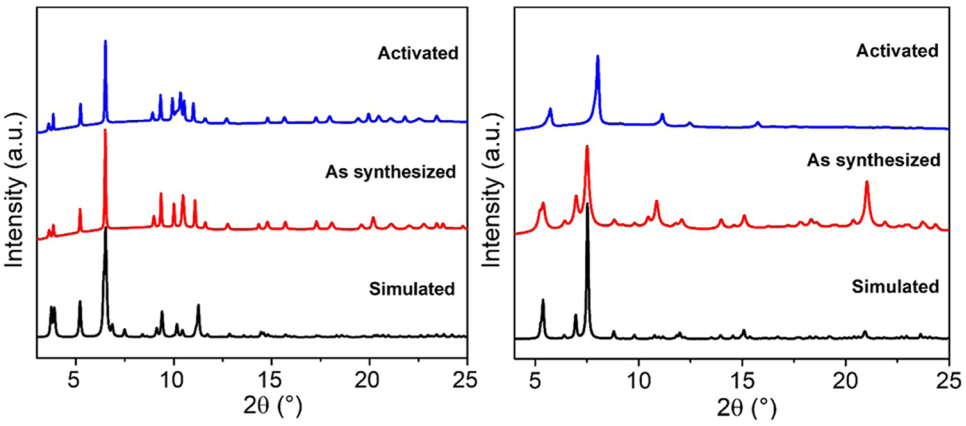

Figure 4. Simulated and experimental PXRD patterns of **1-Nd** MOF (left) and **2-Tb** MOF (right).

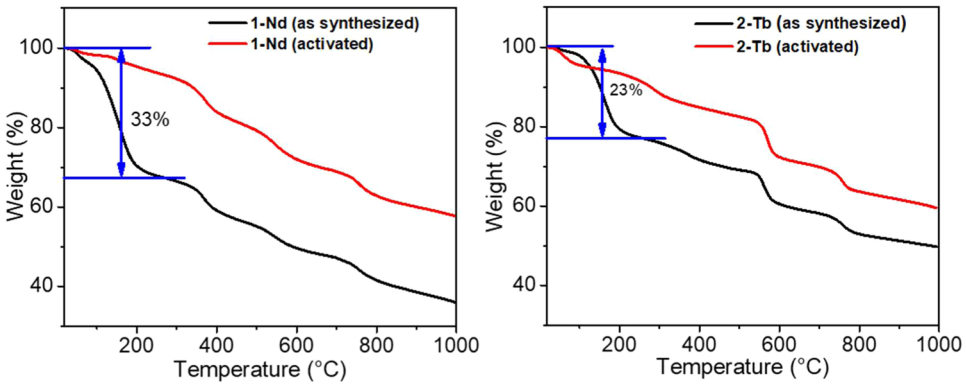

Figure 5. Thermogravimetric plots of **1-Nd** (left) and **2-Tb** (right).

decrease in crystallinity, which is observed as the disappearance of almost all except the main peaks in the diffraction pattern. These peaks are also shifted, signifying contraction of the original unit cell or potential crystal phase transformation, which is discussed in more detail below.

Structural analyses of **1-Nd** and **2-Tb** established that Nd^{3+} and Tb^{3+}—situated rather far apart in the lanthanide series and thus possess rather different ionic radii—give two different MOF structures in the same solvothermal conditions. This prompted us to investigate whether a trend exists within the lanthanide series by synthesizing MOFs using several different Ln^{3+} cations. The PXRD patterns of the MOFs synthesized using early-to-mid lanthanides (La^{3+}, Ce^{3+}, Pr^{3+}, Nd^{3+}, Sm^{3+}, and Eu^{3+}) are consistent with the needle (**1**) phase, while the recorded PXRD patterns of mid-to-late lanthanides (Gd^{3+}, Tb^{3+}, Tm^{3+}, and Yb^{3+}) fit to the plate (**2**) phase (PXRD patterns are shown in Figures S3 and S4). These two structures exhibit two different average coordination numbers (CN) for the lanthanides, 8.7 and 8.0, respectively (8.7 is the average of three different coordination environments in **1-Ln** with CNs eight, nine, and nine). This is consistent with the known trend of aqua ions of Ln^{3+} species as Ln^{3+} ions with large ionic radii (r^{3+} = 1.032−0.947 Å for La−Eu, respectively) prefer the coordination number nine, while coordination number eight is more common for the Ln^{3+} ions with small ionic radii (r^{3+} = 0.938−0.868 Å for Gd−Yb, respectively) with a gradual—rather than sudden—shift in the coordination number in the Eu−Tb region.[43] Earlier literature provides several examples of structural diversity in lanthanide bearing coordination polymers, which arises from the use of Ln^{3+} ions with different ionic radii.[19−22] These studies, which utilize a range of Ln^{3+} cations with differing ionic radii and a variety of carboxylic acid bearing ligands, demonstrate how altering only the lanthanide species can yield two, three, or even four crystallographically different coordination polymers. In three of these four studies, the expected trend of a decrease in the Ln^{3+} coordination number corresponding with a reduction in ionic radii is observed, whereas in the fourth study, the change is indicated by a lesser number of organic ligands in the lanthanide coordination sphere, while the coordination number remains unchanged. In light of these earlier studies, the emergence of the two distinct structure types, with an explicit shift from needle-shaped to the plated-shaped phase without the presence of mixtures at the transition region, is not unexpected.

We also carried out Pawley fitting of the PXRD data to obtain unit cell parameters for the bulk materials. These are presented in Figures S5 and S12 and the refined unit cells in Tables S2 and S3. While there are noticeable differences in the crystallinity of the bulk materials, the refined unit cell parameters are consistent with the above observations and, apart from **1-Ce** and **1-Pr**, show a systematic decrease of unit cell volume fitting well to the contraction of the Ln^{3+} ionic radii. The PXRD pattern of **1-Sm** contains additional peaks at the 9−12° 2θ region, which suggest that the material has undergone partial structural change or there is an additional crystal phase present as an impurity. Furthermore, certain experimental PXRD patterns of the plate-shaped phase (**2-Ln**) show an increased intensity of the (010) and (020) peaks, which can be addressed to flat-plate data collection and light

https://doi.org/10.1021/acs.cgd.5c00153
Cryst. Growth Des. 2025, 25, 3119−3127

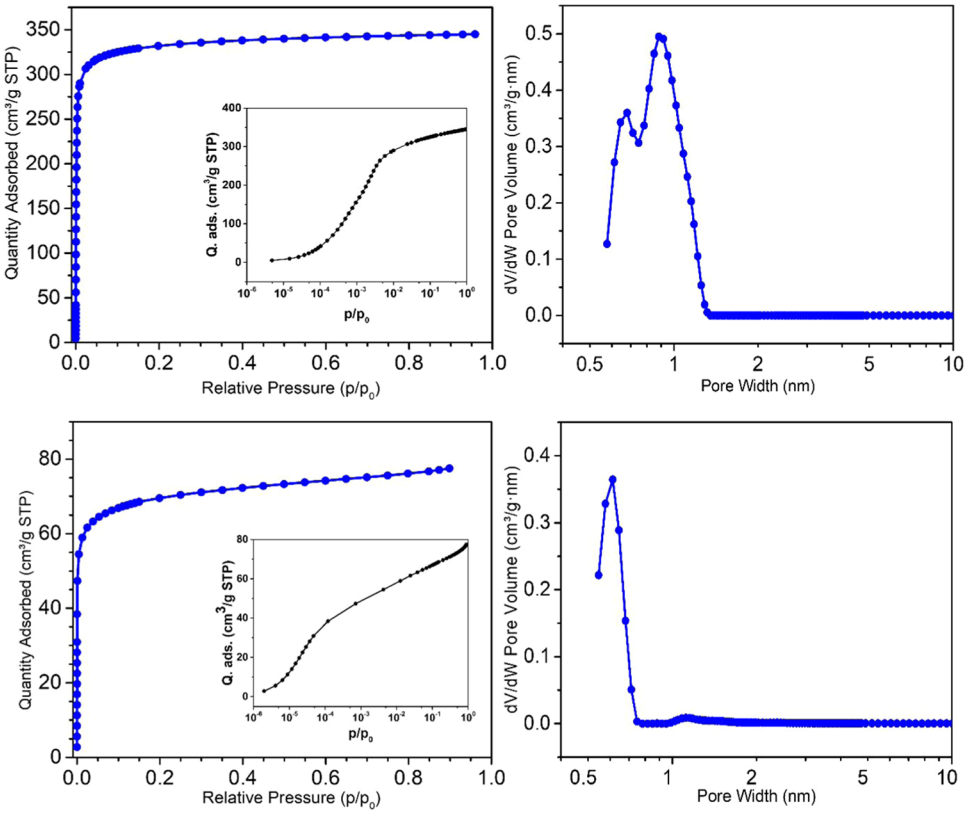

Figure 6. Gas adsorption analysis of **1-Nd** (top) and **2-Tb** (bottom). Left: Argon adsorption isotherms (inset: semilogarithmic display of Ar adsorption). Right: Pore size distributions.

grinding of the plate-shaped crystals, thus causing the preferred orientation.

Thermogravimetric analysis revealed that **1-Nd** and **2-Tb** have similar decomposition profiles (Figure 5). The 33% mass loss between ca. 40 and 240 °C in the **1-Nd** would account for 10 DMF molecules per one TCPP-Fe unit, assuming the pore volume is entirely occupied by DMF rather than a mixture of, for example, DMF and L-proline. Similarly, in **2-Tb**, the most prominent mass loss (23%) occurs between 80 and 240 °C and accounts for ca. 6 DMF molecules. These findings fit well to the estimated number of DMF molecules based on single-crystal structures of these MOFs with void volumes of ca. 1400 and 770 $Å^3$ per respective formula unit. Although significantly smaller, the activated samples also show weight changes at these temperatures, which can be associated with the desorption of adsorbed moisture and potential residual solvent ($CHCl_3$/DMF).[41] Based on the TG curves, the decomposition temperatures for **1-Nd** and **2-Tb** fall within the range of 320−350 °C.

In argon adsorption experiments, the needle-shaped **1-Nd** sample presents a characteristic Type I adsorption isotherm for microporous materials,[44] with a steep initial Ar uptake at low relative pressures filling the micropores, as seen in Figure 6. The apparent surface area can be estimated using the BET method; however, noting that the typical relative pressure range of 0.05−0.3 would not meet the linearity requirement of the BET plot, the applied pressure range has been selected to fulfill the criterion.[45] This provides an apparent surface area of approximately 1223 ± 4 m^2/g, which is very close to the theoretical value of the network-accessible surface area of 1216 m^2/g obtained using a CCDC Mercury pore size analyzer.[46] It is worth noting that there are several inaccuracies when comparing the Ar adsorption isotherms and the calculated results obtained by the pore size analysis tool, including the different interactions of Ar and N_2 with the heterogeneous MOF surface (the latter is used in the calculations) and the difference in the temperature of the X-ray diffraction data collection compared with the gas adsorption measurements. As the adsorption isotherm appears to form a horizontal plateau already at moderate relative pressures, an estimate for the total pore volume would be 0.41 ± 0.01 cm^3/g. Using a zeolite kernel, a pore size calculation using DFT suggests the pores to be 0.6−1.1 nm in diameter (Figure 6). The low limit matches well with the calculated pore limiting diameter (0.56 nm), while the upper limit is clearly higher compared to the calculated value of 0.77 nm. When the theoretical pore sizes are recalculated using the crystal structure with the coordinated water and DMF molecules removed, the calculated values were 0.56 and 0.99 nm, respectively. This suggests that these coordinated solvent molecules are removed upon activation carried prior to the argon adsorption analysis while the structure of **1-Nd** remains unchanged. Compared to **1-Nd**, BET analysis of activated plate-shaped **2-Tb** shows a significantly smaller surface area and pore size. The respective values are 236 m^2/g and 0.6 nm, which are significantly smaller than the calculated values of 919 m^2/g and 0.83 nm, therefore suggesting that **2-Tb** undergoes a structural change prior to these measurements when exposed to high vacuum. This is supported by the PXRD pattern of **2-Tb** after gas adsorption measurements, which shows a significant shift of the main peaks.

Additional stability tests were done to study the behavior of **1-Nd** and **2-Tb** when exposed to atmospheric moisture. Activated samples of **1-Nd** and **2-Tb** were kept under ambient

https://doi.org/10.1021/acs.cgd.5c00153
Cryst. Growth Des. 2025, 25, 3119−3127

atmosphere for 1 month after which the PXRD patterns of both samples were recorded (see Figures S12 and S13). The PXRD patterns show that the crystallinity of **1-Nd** decreases significantly and only the main peak is visible. In contrast, **2-Tb** regains the crystallinity of the pristine (as-synthesized) sample. The relative stability of **2-Tb** over **1-Nd** may be attributed to the protective effect of the low accessible surface area. A similar effect has been reported earlier, notably for SUM-12 and SUM-13, where the surface area has been decreased by the incorporation of long glyme side chains.[47]

CONCLUSIONS

A series of lanthanide-based MOFs were synthesized by a solvothermal method using several different lanthanide Ln^{3+} cations as metal nodes, 5,10,15,20-tetrakis(4-carboxyphenyl)-porphyrin-FeCl as a linker, and L-proline as a coligand. These MOFs crystallized in two different structures, **1-Ln** and **2-Ln**, depending on which lanthanide ion was used. The solvothermal reaction using lanthanides situated on the left-hand side of the lanthanide series (La^{3+}, Ce^{3+}, Pr^{3+}, Nd^{3+}, Sm^{3+}, and Eu^{3+}) gave needle-shaped crystals (**1-Ln**) with the MOF structure consisting of octanuclear Ln_8 rings as discrete SBUs. In the same synthetic conditions, the lanthanides with smaller ionic radii (Gd^{3+}, Tb^{3+}, Tm^{3+}, and Yb^{3+}) yielded crystals with a plate-shaped appearance (**2-Ln**) and structure where the Ln^{3+} ions form infinite 1D SBUs. The average coordination number of the Ln^{3+} ions in **1-Ln** is higher (8.7) compared to **2-Ln** (8.0), and therefore, this structural discontinuity can be explained by the lanthanide contraction, i.e., the contraction of the ionic radius of the Ln^{3+} ions going from left to right in the lanthanide series. Further characterization of these two MOFs, using Nd^{3+} and Tb^{3+} as the selected metal ions, revealed that **1-Nd** is permanently porous with an apparent surface area of 1223 ± 4 m^2/g that corresponds well to the value calculated from the crystal structure. In the case of **2-Tb**, the activation of the material leads to a structural change and a loss of porosity.

To summarize, these results show that L-proline can be used as a coligand in lanthanide-based MOFs, while it may also serve as a modulator. Furthermore, this study highlights that although lanthanide(III) cations are often regarded as a homogeneous group of metal ions in terms of their coordination behavior, they display nuances that warrant their careful examination. We are currently investigating the redox-active, conductive, and magnetic properties of these two MOFs.

ASSOCIATED CONTENT

Supporting Information

The Supporting Information is available free of charge at https://pubs.acs.org/doi/10.1021/acs.cgd.5c00153.

Additional figures (powder X-ray diffraction patterns, SEM micrographs, lanthanide coordination polyhedra), crystallographic information files, crystallographic data tables, and Pawley fitting data (PDF)

Accession Codes

Deposition Numbers 2418331 and 2418332 contain the supplementary crystallographic data for this paper. These data can be obtained free of charge via the joint Cambridge Crystallographic Data Centre (CCDC) and Fachinformationszentrum Karlsruhe Access Structures Service.

AUTHOR INFORMATION

Corresponding Author

Anssi Peuronen − *Department of Chemistry, University of Turku, FI-20014 Turku, Finland;* orcid.org/0000-0002-2504-8196; Email: anssi.peuronen@utu.fi

Authors

Narhari Sapkota − *Department of Chemistry, University of Turku, FI-20014 Turku, Finland*

Ermei Mäkilä − *Department of Physics and Astronomy, University of Turku, FI-20014 Turku, Finland;* orcid.org/0000-0002-8300-6533

Ari Lehtonen − *Department of Chemistry, University of Turku, FI-20014 Turku, Finland;* orcid.org/0000-0002-6958-6519

Complete contact information is available at: https://pubs.acs.org/10.1021/acs.cgd.5c00153

Notes

The authors declare no competing financial interest.

ACKNOWLEDGMENTS

The authors acknowledge the Turku Bioscience Protein Structure and Chemistry Core Facility, a member of Biocenter Finland and FINStruct, for their expertise and for providing access to the single-crystal X-ray diffraction instrument. The authors also acknowledge the Materials Research Infrastructure (MARI) at the Department of Physics and Astronomy, University of Turku, for access and support with the SEM facilities. N.S. gratefully acknowledges the financial support by the Neste and Fortum Foundation.

REFERENCES

(1) Yang, S.; Peng, L.; Syzgantseva, O. A.; Trukhina, O.; Kochetygov, I.; Justin, A.; Sun, D. T.; Abedini, H.; Syzgantseva, M. A.; Oveisi, E.; Lu, G.; Queen, W. L. Preparation of Highly Porous Metal−Organic Framework Beads for Metal Extraction from Liquid Streams. *J. Am. Chem. Soc.* **2020**, *142* (31), 13415−13425.

(2) Jiao, L.; Seow, J. Y. R.; Skinner, W. S.; Wang, Z. U.; Jiang, H.-L. Metal−Organic Frameworks: Structures and Functional Applications. *Mater. Today* **2019**, *27*, 43−68.

(3) Ding, M.; Flaig, R. W.; Jiang, H.-L.; Yaghi, O. M. Carbon Capture and Conversion Using Metal−Organic Frameworks and MOF-Based Materials. *Chem. Soc. Rev.* **2019**, *48* (10), 2783−2828.

(4) Yang, D.; Gates, B. C. Catalysis by Metal Organic Frameworks: Perspective and Suggestions for Future Research. *ACS Catal.* **2019**, *9* (3), 1779−1798.

(5) Dutt, S.; Kumar, A.; Singh, S. Synthesis of Metal Organic Frameworks (MOFs) and Their Derived Materials for Energy Storage Applications. *Clean Technol.* **2023**, *5* (1), 140−166.

(6) Li, B.; Dong, X.; Wang, H.; Ma, D.; Tan, K.; Jensen, S.; Deibert, B. J.; Butler, J.; Cure, J.; Shi, Z.; Thonhauser, T.; Chabal, Y. J.; Han, Y.; Li, J. Capture of Organic Iodides from Nuclear Waste by Metal-Organic Framework-Based Molecular Traps. *Nat. Commun.* **2017**, *8* (1), No. 485.

(7) Sengupta, D.; Melix, P.; Bose, S.; Duncan, J.; Wang, X.; Mian, M. R.; Kirlikovali, K. O.; Joodaki, F.; Islamoglu, T.; Yildirim, T.; Snurr, R. Q.; Farha, O. K. Air-Stable Cu(I) Metal−Organic Framework for Hydrogen Storage. *J. Am. Chem. Soc.* **2023**, *145* (37), 20492−20502.

(8) Cheng, B.; Fu, X.; Song, Y.; Li, Z.; Weng, P.; Yin, X. A Versatile MOF Liquids-Based Janus Fibrous Membrane towards Complex Oil/Water Separation and Heavy Metal Ions Removal. *Sep. Purif. Technol.* **2024**, *331*, No. 125701.

(9) Zhou, Y.; Li, P.; Wang, Y.; Zhao, Q.; Sun, H. Progress in the Separation and Purification of Carbon Hydrocarbon Compounds

Using MOFs and Molecular Sieves. *Separations* **2023**, *10* (10), No. 543.
(10) Li, X.; Lu, S.; Tu, D.; Zheng, W.; Chen, X. Luminescent Lanthanide Metal−Organic Framework Nanoprobes: From Fundamentals to Bioapplications. *Nanoscale* **2020**, *12* (28), 15021−15035.
(11) Zhang, Y.; Liu, S.; Zhao, Z.-S.; Wang, Z.; Zhang, R.; Liu, L.; Han, Z.-B. Recent Progress in Lanthanide Metal−Organic Frameworks and Their Derivatives in Catalytic Applications. *Inorg. Chem. Front.* **2021**, *8* (3), 590−619.
(12) Wang, X.; Jiang, Y.; Tissot, A.; Serre, C. Luminescent Sensing Platforms Based on Lanthanide Metal-Organic Frameworks: Current Strategies and Perspectives. *Coord. Chem. Rev.* **2023**, *497*, No. 215454.
(13) Li, Y.-L.; Wang, H.-L.; Zhu, Z.-H.; Liang, F.-P.; Zou, H.-H. Recent Advances in the Structural Design and Regulation of Lanthanide Clusters: Formation and Self-Assembly Mechanisms. *Coord. Chem. Rev.* **2023**, *493*, No. 215322.
(14) Chen, Y.; Ma, S. Microporous Lanthanide Metal-Organic Frameworks. *Rev. Inorg. Chem.* **2012**, *32* (2−4), 81−100.
(15) Fordham, S.; Wang, X.; Bosch, M.; Zhou, H.-C. *Lanthanide Metal-Organic Frameworks: Syntheses, Properties, and Potential Applications*; Springer: Berlin, Heidenberg, 2014; pp 1−27.
(16) Gorai, T.; Schmitt, W.; Gunnlaugsson, T. Highlights of the Development and Application of Luminescent Lanthanide Based Coordination Polymers, MOFs and Functional Nanomaterials. *Dalton Trans.* **2021**, *50* (3), 770−784.
(17) Zhang, Y.; Zhang, W.; Feng, F.; Zhang, J.; Chen, X. A Highly Connected Porous Coordination Polymer with Unusual Channel Structure and Sorption Properties. *Angew. Chem., Int. Ed.* **2009**, *48* (29), 5287−5290.
(18) Hill, R. J.; Long, D.-L.; Champness, N. R.; Hubberstey, P.; Schröder, M. New Approaches to the Analysis of High Connectivity Materials: Design Frameworks Based upon 4^4 - and 6^3 -Subnet Tectons. *Acc. Chem. Res.* **2005**, *38* (4), 335−348.
(19) Pan, L.; Huang, X.; Li, J.; Wu, Y.; Zheng, N. Novel Single- and Double-Layer and Three-Dimensional Structures of Rare-Earth Metal Coordination Polymers: The Effect of Lanthanide Contraction and Acidity Control in Crystal Structure Formation. *Angew. Chem., Int. Ed.* **2000**, *39* (3), 527−530.
(20) Dimos, A.; Tsaousis, D.; Michaelides, A.; Skoulika, S.; Golhen, S.; Ouahab, L.; Didierjean, C.; Aubry, A. Microporous Rare Earth Coordination Polymers: Effect of Lanthanide Contraction on Crystal Architecture and Porosity. *Chem. Mater.* **2002**, *14* (6), 2616−2622.
(21) Liu, Q.-D.; Gao, S.; Li, J.-R.; Ma, B.-Q.; Zhou, Q.-Z.; Yu, K.-B. Lanthanide Contraction and Anions-Controlled Dimensional Diversity in Ln—Cu—NTA (Ln = lanthanide, H3NTA = nitrilotriacetic Acid) Coordination Polymers: Crystal Structure and Magnetic Properties. *Polyhedron* **2002**, *21* (11), 1097−1103.
(22) He, Z.; Gao, E.-Q.; Wang, Z.-M.; Yan, C.-H.; Kurmoo, M. Coordination Polymers Based on Inorganic Lanthanide(III) Sulfate Skeletons and an Organic Isonicotinate *N* -Oxide Connector: Segregation into Three Structural Types by the Lanthanide Contraction Effect. *Inorg. Chem.* **2005**, *44* (4), 862−874.
(23) Reineke, T. M.; Eddaoudi, M.; Moler, D.; O'Keeffe, M.; Yaghi, O. M. Large Free Volume in Maximally Interpenetrating Networks: The Role of Secondary Building Units Exemplified by $Tb_2(ADB)_3[(CH_3)_2SO]_4\cdot 16[(CH_3)_2SO]$ [1]. *J. Am. Chem. Soc.* **2000**, *122* (19), 4843−4844.
(24) Tang, C.; Li, X.; Hu, Y.; Du, X.; Wang, S.; Chen, B.; Wang, S. Porphyrin-Based Metal-Organic Framework Materials: Design, Construction, and Application in the Field of Photocatalysis. *Molecules* **2024**, *29* (2), No. 467.
(25) Cheng, J.; Zhang, J.; Zheng, S.; Zhang, M.; Yang, G. Lanthanide−Transition-Metal Sandwich Framework Comprising $\{Cu_3\}$ Cluster Pillars and Layered Networks of $\{Er_{36}\}$ Wheels. *Angew. Chem., Int. Ed.* **2006**, *45* (1), 73−77.
(26) Wang, Z.; Li, S.; Wang, Z.; Chen, S.; Wang, F.; Zhang, J. Designing Homochiral Metal−Organic Frameworks with Ultrahigh Surface Areas and Stability for Practical Applications. *Sci. Bull.* **2025**, DOI: 10.1016/j.scib.2025.01.012.
(27) Rhauderwiek, T.; Heidenreich, N.; Reinsch, H.; Øien-Ødegaard, S.; Lomachenko, K. A.; Rütt, U.; Soldatov, A. V.; Lillerud, K. P.; Stock, N. Co-Ligand Dependent Formation and Phase Transformation of Four Porphyrin-Based Cerium Metal−Organic Frameworks. *Cryst. Growth Des.* **2017**, *17* (6), 3462−3474.
(28) Han, Y.; Liu, Z.; Zheng, F.; Bai, Y.; Zhang, Z.; Li, X.; Xiong, W.; Zhang, J.; Yuan, A. Two-Dimensional Flower-like Cobalt-Porphyrin MOF/RGO Composite Anodes for High-Performance Li-Ion Batteries. *J. Alloys Compd.* **2021**, *881*, No. 160531.
(29) Xu, H.-Q.; Hu, J.; Wang, D.; Li, Z.; Zhang, Q.; Luo, Y.; Yu, S.-H.; Jiang, H.-L. Visible-Light Photoreduction of CO_2 in a Metal−Organic Framework: Boosting Electron−Hole Separation via Electron Trap States. *J. Am. Chem. Soc.* **2015**, *137* (42), 13440−13443.
(30) Degen, T.; Sadki, M.; Bron, E.; König, U.; Nénert, G. The HighScore Suite. *Powder Diffr.* **2014**, *29* (S2), S13−S18.
(31) Feng, D.; Gu, Z.; Li, J.; Jiang, H.; Wei, Z.; Zhou, H. Zirconium-Metalloporphyrin PCN-222: Mesoporous Metal−Organic Frameworks with Ultrahigh Stability as Biomimetic Catalysts. *Angew. Chem.* **2012**, *124* (41), 10453−10456.
(32) Hooft, R. *COLLECT*; Nonius BV: Delft, The Netherlands, 1998; pp 1600−5368.
(33) Otwinowski, Z.; Minor, W. [20] Processing of X-ray Diffraction Data Collected in Oscillation Mode. *Methods in Enzymology*; Elsevier B.V., 1997; pp 307−326.
(34) Sheldrick, G. *SADABS*; Bruker AXS Inc.: Madison, Wisconsin, 2002; pp 1600−5368.
(35) Sheldrick, G. M. A Short History of *SHELX*. *Acta Crystallogr., Sect. A: Found. Crystallogr.* **2008**, *64* (1), 112−122.
(36) Sheldrick, G. M. Crystal Structure Refinement with SHELXL. *Acta Crystallogr., Sect. C: Struct. Chem.* **2015**, *71* (1), 3−8.
(37) Dolomanov, O. V.; Bourhis, L. J.; Gildea, R. J.; Howard, J. A. K.; Puschmann, H. OLEX2: A Complete Structure Solution, Refinement and Analysis Program. *J. Appl. Crystallogr.* **2009**, *42* (2), 339−341.
(38) Seaborg, G. T. Actinides and Transactinides. *Kirk−Othmer Encyclopedia of Chemical Technology*; John Wiley & Sons, Inc., 1976.
(39) Bai, K.; Sun, P.; Lassoued, M. S.; Fan, C.; Huang, C.; Zheng, Y.; Chen, W. Effect of Lanthanide Contraction on a Series of "Sulfate-Templated" Transition-Rare-Earth Metal Clusters: Synthesis, Structures and Magnetic Properties. *J. Rare Earths* **2024**, *42*, 2150.
(40) Chandrasekhar, V.; Bag, P.; Colacio, E. Octanuclear $\{Ln(III)_8\}$(Ln = Gd, Tb, Dy, Ho) Macrocyclic Complexes in a Cyclooctadiene-like Conformation: Manifestation of Slow Relaxation of Magnetization in the Dy(III) Derivative. *Inorg. Chem.* **2013**, *52* (8), 4562−4570.
(41) Zhang, H.-D.; Kang, X.; Jing, Y.-T.; Li, H.-Y.; Liang, F.-P.; Huang, F.-P. Two Octa-Nuclear $\{Ln_8\}$ (Ln = Tb, Dy) Complexes with "4 + 4" Covalent Organic Macrocycles: Structure, Solution Behavior, Luminescence, and Magnetic Properties. *Cryst. Growth Des.* **2024**, *24* (7), 2969−2976.
(42) Llunell, M.; Casanova, D.; Cirera, J.; Alemany, P.; Alvarez, S. *SHAPE*, version 2.1; Universitat de Barcelona: Barcelona, Spain, 2013.
(43) Cotton, S. A. Establishing Coordination Numbers for the Lanthanides in Simple Complexes. *C. R. Chim.* **2005**, *8* (2), 129−145.
(44) Thommes, M.; Kaneko, K.; Neimark, A. V.; Olivier, J. P.; Rodriguez-Reinoso, F.; Rouquerol, J.; Sing, K. S. W. Physisorption of Gases, with Special Reference to the Evaluation of Surface Area and Pore Size Distribution (IUPAC Technical Report). *Pure Appl. Chem.* **2015**, *87* (9−10), 1051−1069.
(45) Rouquerol, J.; Llewellyn, P.; Rouquerol, F. Is the BET equation applicable to microporous adsorbents? *Stud. Surf. Sci. Catal.*, **2007**.*160*, 49-56 DOI: 10.1016/S0167-2991(07)80008-5
(46) Macrae, C. F.; Sovago, I.; Cottrell, S. J.; Galek, P. T. A.; McCabe, P.; Pidcock, E.; Platings, M.; Shields, G. P.; Stevens, J. S.; Towler, M.; Wood, P. A. *Mercury 4.0*: From Visualization to Analysis, Design and Prediction. *J. Appl. Crystallogr.* **2020**, *53* (1), 226−235.
(47) Israfilov, N.; Meyer, L.; Feyziyeva, S.; Kyritsakas-Gruber, N.; Louis, B.; Planeix, J.-M. Glyme-Functionalized Ligand Based MOF: A

Comprehensive Study on Copper and Zirconium Frameworks. *J. Solid State Chem.* **2024**, *332*, No. 124582.

https://doi.org/10.1021/acs.cgd.5c00153
Cryst. Growth Des. 2025, 25, 3119−3127